

1 Three-dimensional mapping of mineral in intact shark centra  
2 with energy dispersive x-ray diffraction  
3

4 J.-S. Park<sup>1</sup>, H. Chen<sup>2</sup>, K.C. James<sup>3</sup>, L.J. Natanson<sup>4</sup>, S.R. Stock<sup>5,\*</sup>  
5

6 <sup>1</sup> The Advanced Photon Source, Argonne National Laboratory, Lemont, IL

7 <sup>2</sup> Mineral Physics Inst., Stony Brook Univ., Stony Brook, NY

8 <sup>3</sup> Southwest Fisheries Science Center, National Marine Fisheries Service, NOAA, La Jolla, CA

9 <sup>4</sup> (retired) Northeast Fisheries Science Center, National Marine Fisheries Service, NOAA,  
10 Narragansett, RI

11 <sup>5</sup> Dept. of Cell and Developmental Biology, Feinberg School of Medicine and Simpson Querrey  
12 Inst., Northwestern University, Chicago, IL  
13

14 \* Corresponding author:

15 Mail address: as above 303 E. Chicago Ave., 60611-3008

16 E-mail address: [s-stock@northwestern.edu](mailto:s-stock@northwestern.edu)  
17

Co-author e-mail addresses:

JSP [parkjs@aps.anl.gov](mailto:parkjs@aps.anl.gov)

HC [haiyan.chen@stonybrook.edu](mailto:haiyan.chen@stonybrook.edu)

KCJ [kelsey.james@noaa.gov](mailto:kelsey.james@noaa.gov)

LJN [mangrules@yahoo.ca](mailto:mangrules@yahoo.ca)  
18

19 Abstract: 271 words

20 Text: 7,774 words

21 Figures: 7

22 Tables: 2

23 References: 45  
24

25  
26 **Running title:** 3D energy dispersive diffraction mapping of mineral in shark centra  
27

28  
29 **Disclosures:** The authors have no conflicts of interest.  
30

31

32 **Abstract**

33 The centra of shark vertebrae consist of cartilage mineralized by a bioapatite similar to bone's  
34 carbonated hydroxyapatite, and, without a repair mechanism analogous to remodeling in bone,  
35 these structures still survive millions of cycles of high-strain loading. The main structures of the  
36 centrum are an hourglass-shaped double cone and the intermedialia which supports the cones.  
37 Little is known about the nanostructure of shark centra, specifically the relationship between  
38 bioapatite and cartilage fibers, and this study uses energy dispersive diffraction (EDD) with  
39 polychromatic synchrotron x-radiation to study the spatial organization of the mineral phase and  
40 its crystallographic texture. The unique energy-sensitive detector array at beamline 6-BM-B, the  
41 Advanced Photon Source, enables EDD to quantify the texture within each sampling volume  
42 with one exposure while constructing 3D maps via specimen translation across the sampling  
43 volume. This study maps a centrum from two shark orders, a carcharhiniform and a lamniform,  
44 with different intermedialia structures. In the blue shark (*Prionace glauca*, Carcharhiniformes),  
45 the bioapatite's *c*-axes are oriented laterally within the centrum's cone walls but axially within  
46 the wide wedges of the intermedialia; the former is interpreted to resist lateral deformation, the  
47 latter to support axial loads. In the shortfin mako (*Isurus oxyrinchus*, Lamniformes), there is  
48 some tendency for *c*-axis variation with position, but the situation is unclear because one  
49 dimension of the sampling volume is considerably larger than the thickness and spacing of the  
50 intermedialia's radially-oriented lamellae. Because elastic modulus in collagen plus bioapatite  
51 mineralized tissues varies significantly with both volume fraction of bioapatite and  
52 crystallographic texture, the present 3D EDD-derived maps should inform future 3D numerical  
53 models of shark centra under applied load.

54

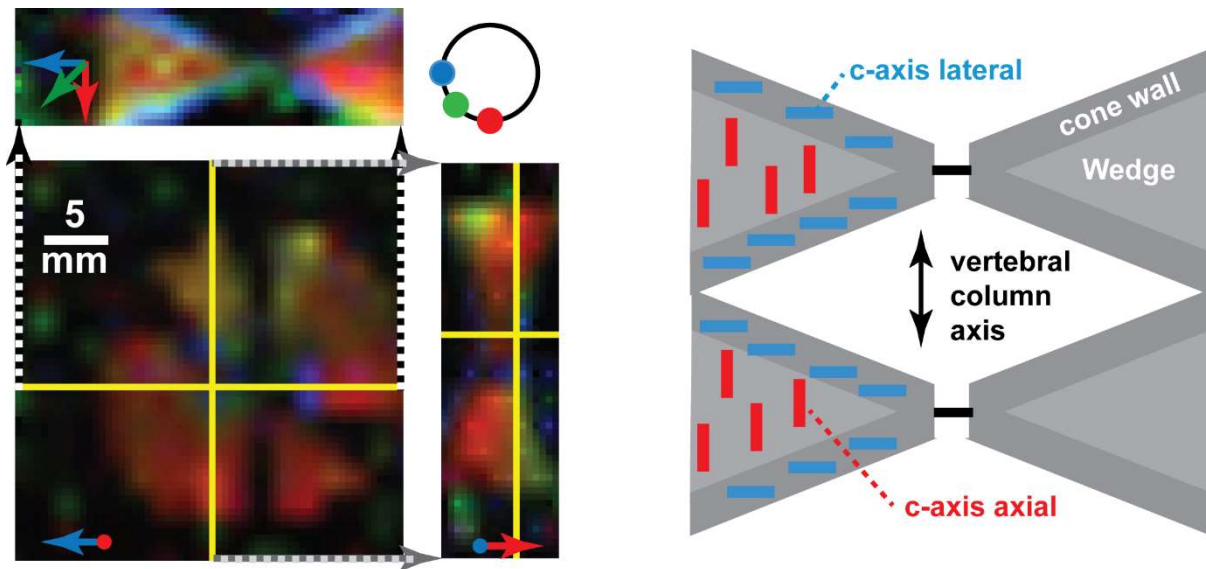
55 **Keywords:** energy dispersive diffraction; bioapatite (hydroxyapatite); shark; centrum;  
56 mineralized cartilage; crystallographic texture

57  
58  
59  
60  
61  
62  
63  
64  
65  
66  
67  
68  
69  
70  
71  
72  
73  
74  
75

### Highlights

- Energy dispersive diffraction mapped, in 3D, bioapatite diffracted intensity/crystallographic texture in shark vertebra.
- In one subvolume (cones), blue shark bioapatite *c*-axes were oriented laterally and elsewhere (intermedialia) axially.
- The blue shark crystals appear oriented to resist lateral deformation (cone) and to support axial loads (intermedialia).
- The shortfin mako's *c*-axis orientation varied with position, but a relationship with microstructure was unclear.
- Incorporation of EDD-derived crystallographic texture into 3D models of shark centra are discussed.

### Graphical Abstract



**Bioapatite crystal orientations in blue shark centrum. (left) Energy dispersive diffracted intensity in 3D (colors indicate intensity along different anatomical directions). (right) Schematic indicating crystal *c*-axes in different portions of the centrum.**

76

77 **Introduction**

78           Elasmobranchii, which include sharks, rays and skates, have cartilaginous skeletons, and  
79 relatively little is known (either experimentally or numerically) about how their subcranial axial  
80 skeletons function under in vivo loads. The sharks studied by Natanson et al. (2018)  
81 (elasmobranch orders Carcharhiniformes and Lamniformes) possess more than 80 vertebrae (Fig.  
82 1a), each with a mostly unmineralized neural arch and a mineralized centrum, and these sharks'  
83 abdominal centra carry the loads generated during swimming (Porter and Long 2010). When a  
84 shark swims, its tail beats from left to right, compressing first one side then the other side of each  
85 centrum (Fig. 1b), and the magnitude increases from the juncture of the thorax and abdomen  
86 toward the tail. The structure and mineralization of the carcharhiniform and lamniform centra  
87 enables shark vertebrae to survive enormous compressive strains of 3-8% (Porter et al. 2014) for  
88 millions of cycles of loading (Watanabe et al. 2012), despite the absence of a repair mechanism  
89 like remodeling in bone.

90           Shark centra have complex 3D structures affecting mechanical performance, and there  
91 are significant similarities and important differences between carcharhiniform and lamniform  
92 centra. The centra of both orders contain an hourglass-shaped double cone of mineralized  
93 cartilage (Fig. 1c) termed the corpus calcarea. A fluid filled inter-vertebral capsule lies between  
94 the cone walls of adjacent vertebrae. Within a single centrum, the rostral and caudal cone walls  
95 are supported by the mineralized intermedialia whose structure differs between the two orders  
96 (Fig. 1c). In Carcharhiniformes, the intermedialia consists of four thick wedges (Fig. 1d) with  
97 unmineralized (cartilage) gaps separating the wedges. In Lamniformes, two dozen or more,  
98 relatively thin, radially-oriented plates (lamellae) comprise the intermedialia (Fig. 1d); these  
99 lamellae may be distinct from each other or may combine and separate from their neighbors, e.g.

100 the one o'clock position of the left side of Fig. 1d and Morse et al. (2022). The lamellae are  
101 grouped into four sectors separated by four gaps; two sectors are wider and contain more  
102 lamellae than the other two sectors. In both carcharhiniforms and lamniforms, the cartilage of  
103 one pair of gaps extends to form the neural arch and that of the other pair to form the hemal arch  
104 (if present).

105         During swimming, both the left and right sides of shark abdominal centra experience an  
106 alternating pattern of compression and tension. Some studies of the macroscopic patterns of  
107 strain in the shark vertebral column have appeared (Porter and Long 2010; Porter et al. 2014,  
108 Porter et al. 2016), but little is known about the 3D distributions of displacement or of strain  
109 within the complex structure of a shark centrum. Experimental measurement of these 3D strains  
110 under applied load is one way forward and is, in fact, an eventual goal of the authors, see the  
111 preliminary report of Park et al (2022c). An alternative to understanding centrum function is 3D  
112 numerical modeling which requires accurate geometrical and materials property inputs, and  
113 obtaining some of this information is the focus of the present report. Beyond the centra  
114 macrostructure (3D geometry at the  $\sim 50 \mu\text{m}$  and higher scales), mineral density, microstructure  
115 (scales  $1 \mu\text{m}$  and above) and nanostructure (scales  $0.1 \text{ nm}$  and higher) contribute to functionality.  
116 These centra structural levels are not independent, and, before introducing the energy-dispersive  
117 x-ray diffraction-based nanostructural studies of this paper, prior studies of centra macrostructure  
118 and microstructure are reviewed.

119         Macrostructure of entire lamniform and carcharhiniform centra have been studied with  
120 microComputed Tomography (microCT) with volume elements (voxels)  $> 15 \mu\text{m}$ , e.g. Geraghty  
121 et al. (2012), Natanson et al. (2018) and Morse et al. (2022). The last study found mineral levels  
122 in the cone wall were significantly greater than in the intermedialia. As elastic moduli increase

123 with increasing mineral content in collagen-based tissues (Currey 2002), such mineral content  
124 variation in centra should be incorporated into qualitative and/or quantitative models of response  
125 to applied loads. Microstructure in small blocks cut from centra have been studied with microCT  
126 with voxels  $\sim 1 \mu\text{m}$  in size (Stock et al. 2022), these very limited data need to be supplemented  
127 before they can reliably guide understanding of mechanical properties. Nanostructure also affects  
128 properties, and the focus here is on the nanocrystals of the mineral phase and the crystallographic  
129 orientation of the mineral within the cartilage matrix. Data on bone suggests that mineralized  
130 tissues consisting of collagen reinforced by bioapatite often contain a mineral phase where  
131 certain crystal axes are strongly oriented relative to anatomical axes of principal in vivo stresses,  
132 i.e., contain crystallographic texture (Currey 2002), and that this texture is strong enough to  
133 produce significant variation in elastic constant as a function of orientation (Guo 2001). Failure  
134 to incorporate such elastic modulus variation, if present in shark centra, into interpretation of  
135 mechanical tests or in 3D modeling of shark centra may lead to inaccurate conclusions. Although  
136 microstructural, micromechanical and histological studies have appeared on the mineralized  
137 cartilage of shark tesserae, e.g. Chaumel et al. (2020) and Seidel et al. (2019, 2021), which is a  
138 rather different tissue from that of the centra, crystallographic data are sparse for tesserae. Some  
139 data, however, are available on shark bioapatite.

140         An early diffraction study (Urist 1961) showed that the centra's mineral is a bioapatite  
141 closely related to hydroxyapatite (hAp), and TEM showed a similar bioapatite in shark tesserae  
142 (Dean et al. 2005). Recently Park et al. (2022a) used monochromatic synchrotron x-radiation to  
143 collect diffraction patterns from small blocks cut from centra of four species and confirmed that  
144 the only crystalline phase visible was a bioapatite with lattice parameters slightly different from  
145 those of bone and stronger crystallographic texture than in mammalian long bones. This latter

146 study, however, was not designed to compare texture from different portions of the centra, and  
147 3D mapping of centrum texture is the focus of the present study.

148         The present authors hypothesize that, like the collagen fibril (type I collagen) and  
149 bioapatite orientations in long bones, the cartilage (2/3 collagen type II, 1/3 collagen type I plus  
150 significant proteoglycans) fiber axes and bioapatite crystal *c*-axes in shark centra are aligned  
151 along the direction(s) of principal strain and that these directions may vary with position within  
152 the centrum. The study reported below, performed at beamline 6-BM-B of the Advanced Photon  
153 Source (APS), employs energy dispersive x-ray diffraction (EDD) and a unique array of energy  
154 sensitive detectors (Weidner et al. 2010) to obtain 3D position resolved diffraction maps of two  
155 shark centra. The maps are obtained by X, Y and Z translation of the specimen across the  
156 sampling volume and without sample rotation. Alternative EDD data collection strategies have  
157 been used in the past, e.g. to study cement paste degradation due to sulfate attack (Naik et al.  
158 2006) and to study the cross-section of bones (Stock et al. 2017), but the present instrument  
159 allows direct quantification of the 3D variation of crystallographic quantities (intensity of  
160 diffraction peaks, lattice parameters, crystallite size/microstrain, texture) within specimens.  
161 Alternative 3D diffraction mapping methods using monochromatic x-ray are available and are  
162 contrasted with this EDD approach in the Discussion.

163         This paper reports 3D EDD-derived maps of a carcharhiniform shark and a lamniform  
164 shark. Maps of mineral content are already available for intact centra (Morse et al. 2022), and the  
165 focus here is on crystallographic texture, something the authors expect will be essential to  
166 accurate 3D numerical modeling. Incorporation of texture and of mineral content into 3D models  
167 is also discussed.

168

169 **Materials and Methods**

170 One abdominal vertebrae of a species of Carcharhiniformes (*Prionace glauca*, blue shark,  
171 from vertebra numbers 81-84) and one of a species of Lamniformes (*Isurus oxyrinchus*, shortfin  
172 mako, vertebra number 62) were examined in this study. Laboratory microCT (Morse et al.  
173 2022) showed the diameter and height were diameter 24.3 mm and 12.7 mm, respectively, for  
174 the blue shark centrum and 21 mm and 12.4 mm, respectively, for the shortfin mako centrum.  
175 Figure 1c shows 3D schematics of the two types of centra with the material closest to the viewer  
176 rendered transparent so the inner structure could be seen. Figure 1d shows transverse sections  
177 through the axial midplane of each centrum with the mineralized tissue shown in black.

178 The experimental geometry for EDD at beamline 6-BM-B, APS, is shown in Fig. 2a  
179 (Weidner et al. 2010). A collimator forms a pencil beam of polychromatic radiation which passes  
180 through the specimen (a schematic transverse section near the middle of a shortfin mako  
181 centrum). The conical receiving slits block all radiation except that diffracted from the sampling  
182 volume “sv” at an angle  $2\theta = 6.5^\circ$ . Linear translators move the sample across the sampling  
183 volume along the three orthogonal axes X (horizontal, perpendicular to the incident beam), Y  
184 (vertical, perpendicular to the incident beam) and Z (horizontal, parallel to the incident beam).

185 Bragg’s law,  $\lambda = 2 d_{hk.l} \sin \theta$ , gives the angle  $\theta$  at which peaks of diffracted intensity  
186 occur from crystalline material and shows that this angle depends on the x-ray wavelength (i.e.,  
187 the inverse of the x-ray energy) and the crystal periodicity or d-spacing  $d_{hk.l}$  for lattice planes  
188  $hk.l$ .<sup>1</sup> With the Bragg angle fixed ( $2\theta = 6.5^\circ$ ), a range of energies in the polychromatic beam and  
189 an array of differently oriented crystals with the sampling volume sv, different  $hk.l$  select  
190 different energies and produce diffracted beams which reach one of the ten energy sensitive

---

<sup>1</sup> Here the abbreviated Miller-Bravais indexing system is used to emphasize the hexagonal crystal system of hAp (Cullity and Stock 2001).



191 detectors of the 6-BM-B array (Fig. 2b). For the bioapatite in the shark centra, each detector  
192 measures the intensity of 00.2 diffraction of  $\sim 32$  keV x-rays as well as the intensity of the  
193 unresolved quadruplet of 21.1, 11.2, 30.0 and 20.2 of 38-42 keV x-rays and other reflections that  
194 might be intense enough to pick out from the background. Note that the orientation of the  
195 crystals diffracting into detector 5 is given by orientation of lattice plane normal  $\mathbf{N}_5$  which makes  
196 an angle  $(90 - \theta)^\circ$  from both the incident beam  $\mathbf{S}_0$  and the diffracted beam direction  $\mathbf{S}_5$  and which  
197 lies in the horizontal plane (Fig. 2b). The same is true each other detector, i.e., for detector 1,  
198 normal  $\mathbf{N}_1$ ,  $\mathbf{S}_0$  and the diffracted beam direction  $\mathbf{S}_1$  are coplanar (vertical plane) and make the  
199 same angles. Therefore, comparison of 00.2 diffracted intensities between different detectors  
200 gives the relative fractions of crystalline bioapatite with different orientation defined by their  
201 lattice normal orientations  $\mathbf{N}_i$ , i.e., the crystallographic texture within the sampling volume sv.

202 Figure 2c shows two views of the shortfin mako centrum (the side view in the top panel  
203 and the central transverse section in the bottom panel). Figure 2d shows the same views of the  
204 blue shark centrum. The red squares indicate extent of the specimen covered by the sampling  
205 volumes; note that neither the spacing between sampling volumes nor their dimensions are to  
206 scale.

207 Table 1 gives the experimental parameters for the scans of the two sharks. For the blue  
208 shark and shortfin mako, the pencil beam dimensions were  $\delta X = 0.1$  mm and  $\delta Y = 0.2$  mm and  
209  $\delta X = \delta Y = 0.2$  mm, respectively. A  $\sim 0.9$  mm thick powdered ceria standard (NIST SRM 674B)  
210 was scanned across the sampling volume, and the full-width at half-maximum of the diffracted  
211 peak intensities was used as the measure of the gage length  $\delta Z$  along the incident beam direction.  
212 The gage lengths for the different detectors varied slightly (see Supplemental Fig. S1, mean of  
213  $\sim 1.7 \pm 0.15$  mm) and sampled the same position within  $\sim 0.25$  mm; these uncertainties are much

214 smaller than those from other sources and are hereafter ignored. For the beam dimensions used  
215 to map the blue shark centrum,  $\delta Z$  averaged 1.7 mm, and for the shortfin mako,  $\delta Z$  averaged 2.5  
216 mm. The translation step sizes used to build up the 3D maps were  $\Delta X = 2.0$  mm,  $\Delta Y = 1.0$  mm  
217 and  $\Delta Z = 1.9$  mm for the blue shark centrum and were  $\Delta X = 1.5$  mm,  $\Delta Y = 0.5$  mm and  $\Delta Z = 1.0$   
218 mm for the shortfin mako. Note that the entire volume of the blue shark centrum was scanned  
219 (diameter 24.3 mm, height 12.7 mm), but only a portion of the shortfin mako centrum (diameter  
220 ~21 mm, height 12.4 mm) was covered. For both centra, the 3D reconstruction on a 0.5 mm x 0.5  
221 mm x 0.5 mm grid with interpolation of the neighboring volume elements (voxels) with  
222 smoothing.

223         As noted in the previous paragraph, data collection parameters (and fraction of centrum  
224 covered) differed for the two centra. Point by point mapping of 3D volumes is quite time  
225 consuming: Ignoring motion and detector readout overhead, collecting the  $16 \times 10 \times 17 = 2,720$   
226 patterns covering the blue shark centrum required 22.7 hr, and collecting the  $3 \times 10 \times 47 = 1,410$   
227 patterns covering a portion of the shortfin mako centrum required 19.6 hrs. Limited beam time  
228 (typically 4 days per scheduling cycle) dictated, therefore, that the sampling parameters were  
229 altered match centra characteristics while not exhausting available time. Given the blue shark  
230 intermedialia consisted of wedges, a relatively uniform sampling grid was selected at the cost of  
231 spatial resolution. Because the mako's intermedialia consisted of relatively thin lamellae  
232 compared to the sampling volume dimension along the incident beam direction Z, sampling  
233 along the beam direction was increased substantially compared to the blue shark, thereby  
234 improving the chances that individual lamellae could be resolved, at the cost of decreasing the  
235 volume scanned along X and Y.

236 The energy range of each detector was simultaneously calibrated using an array of ten,  
237 pre-aligned  $^{57}\text{Co}$  sources. As mentioned above, a ceria standard was used to measure the  
238 sampling volume length along the beam direction. The  $d$ -spacings of the known ceria diffraction  
239 peaks were also used to confirm the linearity of the energy range.

240 The integrated intensity and position for each peak (00.2 and q) were determined by  
241 fitting a pseudoVoigt function (custom Matlab scripts). For each point-wise data set, integrated  
242 peak intensity for each peak (measured by each detector element in the detector array) was  
243 interpolated and smoothed using a  $0.5\text{ mm} \times 0.5\text{ mm} \times 0.5\text{ mm}$  grid using Matlab  
244 *scatteredInterpolant* function with default parameters. The interpolated 3D maps were imported  
245 into ImageJ as a stack of slices and viewed with the orthogonal views function. Intensity maps  
246 from different detectors were combined using the color/merge function of ImageJ.

247

## 248 **Results**

249

250 Figure 3 shows a diffraction pattern (intensity vs x-ray energy) typical of a shark centra.  
251 Calibration lines from radioactive sources appear at high and low energies and are labeled “cal”.  
252 Two bioapatite reflections are labeled 00.2 and “q”, i.e., the closely spaced and unresolved  
253 quadruplet of 21.1, 11.2, 30.0 and 20.2. In Fig. 3, the maximum 00.2 and q peak intensities were  
254  $\sim 150$  cts and  $\sim 430$  cts above background, respectively (compared to backgrounds of  $\sim 100$  cts  
255 and  $\sim 120$  cts, respectively). Two sections of the pattern are plotted in red; this is the energy  
256 range over which the 00.2 and quadruplet integrated intensities are calculated. The green peaks  
257 below the experimental data show peaks expected for a synthetic hAp reference pattern (Powder  
258 Diffraction File 86-1201, International Centre for Diffraction Data, Newtown, PA, USA), and  
259 there is a clear difference of in energy diffracted by each  $hk.l$  (the green peak reference position

260 vs red highlighted experimental data from a centrum), and, hence, a small but significant  
261 difference in lattice parameters. The ratio of 00.2 to q peak intensities in Fig. 3 is 35%,  
262 somewhat lower than the 45% ratio expected for the crystallographic-texture-free powder of PDF  
263 86-1201.

264

### 265 Blue shark

266 Figure 4 shows orthogonal sections through the 3D reconstructed volume of the blue  
267 shark centrum using the integrated intensity of reflection q (unresolved 21.1+11.2+03.0+20.2).  
268 Within each panel, the three sub-panels show orthogonal sections, the square sub-panels being  
269 the transverse section through the axial center of the centrum and the yellow lines and arrows  
270 indicating the sections' positions in the 3D volume. In the top row, the left panel (labeled 5) is  
271 the reconstruction using intensities from detector 5), and the middle panel is intensities from  
272 detector 10, diametrically opposite detector 5. The right panel of the top row of Fig. 4 shows a  
273 composite of the two reconstructions with detector 5 intensities shown in blue and detector 10  
274 intensities shown in red. The reconstructed transverse cross-sections look like the lab microCT  
275 reconstruction in Fig. 1d, if one allows for the lower spatial resolution of the EDD data.

276 The left panel of the bottom row of Fig. 4 plots intensities from detector 1, the middle  
277 panel plots intensities of detector 9 (diametrically opposite detector 1) and the right panel shows  
278 a composite with detector 1 intensity shown in red and detector 9 in blue. Although there are  
279 regions of red in the 1+9 composite panels, most of the volume appears magenta, i.e., more or  
280 less even intensities of the two opposite orientation detectors. In the composite 5+10, most of the  
281 volume is magenta but the regions of red intensity are more prominent at the margins of the  
282 mineralized tissue.

283 At some positions in longitudinal sections (those parallel to the centrum's axis and  
284 running horizontally in Fig. 4), the integrated intensity of the  $q$  reflection is greater than in the  
285 neighboring volume (yellow arrowheads); the higher intensity corresponds to the location of the  
286 cone walls and the lower to intermedialia (Morse et al. 2022). In other portions of the same  
287 sections, there is little difference in  $q$  intensity across the section (orange arrowheads). Table 2  
288 gives values of the mean integrated intensity (and its standard deviation given after the  $\pm$   
289 symbol) within the  $3 \times 3$  voxel boxes within the cone wall and intermedialia. Inspection reveals  
290 that the intensities vary within the intermedialia, and boxes  $i$  and  $i'$  were measured and show  
291  $\sim 50\%$  variation (Table 2).

292 Crystallographic texture in mineralized tissues containing bioapatite typically manifests  
293 in differences in 00.2 diffracted intensity along different anatomical directions. Figure 5, also of  
294 the blue shark centrum, shows three orthogonal sections through the 00.2 intensity reconstructed  
295 volume. In Fig. 5a, diffracted intensity from detector 5 is shown in blue, that from detector 7 in  
296 green and that from detector 9 in red. The colored arrows in each panel indicate the direction of  
297  $c$ -axis crystallites sampled by the respective detector. Before describing what the different colors  
298 within the sections reveal, it is useful to consider the magnitude of the integrated intensities  
299 (Table 2). The largest integrated intensity within this 00.2-reconstructed volume is 86 arbitrary  
300 units (a.u.) and the mean value within a  $3 \times 3$  voxel box within fluid ("f" in Fig. 5a) is 2 a.u.  
301 Within the sampling box in the cone wall, the mean 00.2 integrated intensity was  $46 \pm 9$  a.u. for  
302 detector 5 and  $21 \pm 5$  a.u. for detector 1 (the direction equivalent to the detector 9 data plotted).  
303 Within the sampling box in the intermedialia, the detector 5 intensity is  $5 \pm 1$  a.u. and detector 1  
304 intensity is  $35 \pm 2$  a.u.

305           The transverse section through the middle of the centrum (the square image, lower left  
306 panel of Fig. 5a) has an intensity distribution like the transverse section shown in Fig. 1d, and,  
307 over most of the cross-section, the crystallites have *c*-axes oriented axially (red color indicating  
308 bioapatite *c*-axes primarily normal to the transverse plane, see coordinate axes at the lower left of  
309 this panel). In the side-view cross-section (upper panel of Fig. 5a) the blue voxels represent hAp  
310 crystallites with their *c*-axes oriented to diffract along the X direction (blue arrow), i.e., laterally  
311 (radially) in relation to the backbone axis, and the red voxels show crystallites with *c*-axes  
312 aligned axially. In the section of the right-hand panel of Fig. 5a, little blue appears; in this section  
313 blue indicates *c*-axis orientations out of the plane of this section and along the hoop  
314 (circumferential) direction; therefore, indicating large fractions of the hAp crystallites in the cone  
315 wall are not correctly oriented to diffract in the directions viewed by the respective detectors.  
316 Figure 5b schematically indicates observations shown in Fig. 5a: lateral (radial) *c*-axis  
317 orientations in the cone walls and axial orientations in the wedge between the cone walls  
318 (intermedialia).

319

### 320 Shortfin mako

321           Figure 6 shows reconstructed transverse sections (diffracted intensity vs position) for all  
322 ten detectors; maps for reflection *q* appear in (a) and for 00.2 appear in (b). A segmented lab  
323 microCT section of the mako centrum, at approximately the same axial position as the EDD  
324 maps and with the same orientation, is inset in the middle of the detector images in Fig. 6a. Gaps  
325 *g*1 and *g*2 between sectors can be resolved in all of the EDD maps and can be matched to *g*1 and  
326 *g*2 in the lab microCT-derived image. A small part of a wide sector *s*1, which borders gap *g*1,  
327 appears at the top of the maps in Fig. 6; the scan covers the outer ~3 mm of the radial lamellae.

328 A significant portion of sector s3 appears below gap g2, and each panel shows 4 mm of sector s2,  
329 excluding the outer-most and inner-most portions of the lamellae.

330 The spatial distribution of q reflection intensities is the same for all of the detectors (Fig.  
331 6a). The magnitude of intensities differs somewhat; they are greater for detectors 1-4 than for 6-9  
332 and are larger for detector 5 than for the diametrically opposite detector 10. The sectors' borders  
333 with the gaps have higher intensity than positions between the borders, consistent with the much  
334 closer spacing of lamellae in these locations seen in microCT, i.e., the image in the center of Fig.  
335 6a and in Morse et al. (2022). The intensity map of sector s2, for example, shows two radial  
336 bands of increased intensity separated by a region of lower intensity. Away from its border with  
337 the gap, the reconstructed portion of sector s3 contains three distinct bands radiating from the  
338 middle of the centrum (indicated by the red arrows in the detector 8 map of Fig. 6a); the  
339 intensities of these bands are substantially lower those bordering the gaps.

340 Outside of the centrum, the q intensity within the fluid is mostly below 100 a.u. although  
341 there are scattered points where the measured intensity reaches 300 a.u. The maximum intensity  
342 for this volume for all detectors is 1,200 a.u. Within s1, the intensities approach about 900 a.u.  
343 for detector 1 and for 800 a.u. in detector 5. In the detector 1 map, the maximum intensities are  
344 somewhat larger (~1,000 a.u.) within the 10 o'clock and 9 o'clock oriented radial lamella(e) of  
345 s2 with the in-between volume having an intensity ~500 a.u. In the detector 5 map, the intensity  
346 of the 10 o'clock lamella(e) is about 800 a.u. and somewhat larger than that in the 9 o'clock  
347 band.

348 In many respects, the spatial distribution of 00.2 diffracted intensities mirrors that of the q  
349 reflection maps. The radial bands bordering the gaps have higher intensities than sectors'  
350 material between the gaps, but the three radial bands at the bottom of sector 3 are less clearly

351 defined for 00.2 than for q. The 00.2 intensities in the maps of detectors 4-6 are much greater  
352 than those collecting intensities at azimuths 90° away (detectors 1 and 2 and 8 and 9) and 180°  
353 away (detector 10). Further, the intensities in detector 1 and 2 maps are greater than those at  
354 corresponding positions in the 8 and 9 maps.

355         The maximum 00.2 integrated intensity for this volume for all detectors is 150 a.u., and  
356 the volumes containing only fluid (bottom area of the maps, below s3) are quite noisy intensity  
357 maps reflecting the especially poor counting statistics. Maximum intensity within the 10 o'clock  
358 orientated lamella(e) is about 90 a.u. in the detector 2 map and about 120 a.u. in the 9 and 10  
359 o'clock lamella(e) with lower intensities between the two. The base of the s3 band (right hand  
360 side of the map, 8 o'clock orientation) has an intensity of 60 a.u. for detector 3 whereas the  
361 intensity is 70 a.u. in the detector 5 map.

362  
363

## 364 **Discussion**

365  
366         There are at least two contexts where the EDD results reported above would be of interest

367 to readers of a journal concerned with mechanical behavior. First, the successful EDD mapping  
368 in this paper is a precursor to 3D mapping of internal strains arising from in situ loading of shark  
369 centra. Second, the 3D mapping of various bioapatite characteristics (notably crystallographic  
370 texture) is essential input for accurate modeling. Before discussing the present EDD data and  
371 considering how these might apply in these two contexts, it is important to summarize what is  
372 known about the tissue most closely related to that of the shark centra, i.e., tessellated cartilage  
373 of sharks and related elasmobranchs, and to review prior mechanical behavior studies of centra.

374

375 *Tessellated cartilage of sharks and related species related to centra tissue*



376 To date, tessellated cartilage has received much more attention than the mineralized  
377 cartilage of centra and, and these data may or may not guide understanding of centra mechanical  
378 functionality. In polished sections of dry stingray tesseræ, Seidel et al. (2019) found different  
379 regions possess different mineral densities and nanoindentation hardnesses which they related to  
380 mechanical functionality. Seidel et al. (2019) correlated tesseræ mineral density with  
381 nanoindentation hardness and found that stingray mineralized cartilage had a higher mineral  
382 content than reported by Gupta et al. (2005) for calcified human cartilage, but the relationship of  
383 Young's modulus to mineral content for tesseræ was consistent with an extrapolation from data  
384 for human calcified cartilage.

385 Elasmobranch tesseræ contain chondrocyte lacunae and canaliculi, but most of their  
386 volume is dense mineralized cartilage, at least at the one-micrometer level. In stingray tissue, for  
387 example, the lacunae average 6-7 vol%, and the canaliculi may add an additional couple vol%  
388 porosity (Chaumel et al. 2020). This tissue microstructure is quite different from that of shark  
389 centra, e.g. Fig. 5 of Stock et al. (2022): from this image, the present authors estimate ~76 vol%  
390 pores/soft tissue and 3-4.5  $\mu\text{m}$  trabeculae thickness for the intermedialia volume and 59 vol%  
391 pores/soft tissue and ~8  $\mu\text{m}$  trabeculae thickness for the cone wall volume. Even if the  
392 mineralized cartilage constitutive properties (mineral content, elastic moduli, yield stress,  
393 fracture toughness, ...) are the same at the 50-1,000 nm scale for both tissues, the very different  
394 microarchitectures of tesseræ and centra suggest very different mechanical properties at scales  
395 one micrometer and above.

396

397 *Prior studies of centra mechanical behavior*

398           Before discussing prior studies of mechanical functionality of centra, it is useful to  
399 consider what is known about the mechanical properties of tessellated tissue, the tissue most  
400 closely related to that of centra. Liu et al. (2014) applied compressive loading normal to and  
401 parallel to the plane of blue shark jaw tesseræ surrounded by uncalcified cartilage; their focus  
402 was measuring and modeling stress relaxation behavior during in vivo biting and their values of  
403 elastic moduli are informative for the unmineralized cartilage but not for mineralized tesseræ.  
404 One way to isolate the calcified tissue is to produce polished sections of tesseræ and perform  
405 nanoindentation, and, depending on the position within stingray tesseræ, the resulting Young's  
406 moduli range from 15 to 35 GPa for tissue densities 1.5 to 2.7 g/cm<sup>3</sup>, respectively (Seidel et al.  
407 2019), which on average are higher than in human cortical bone (Guo 2001).

408           Porter and Long (2010) tested vertebrae (neural arch plus centrum, centrum alone) from a  
409 carcharhiniform shark in uniaxial compression and determined that the arch did not carry  
410 appreciable load. The experimental Young's modulus determined was ~150 MPa which  
411 combines the tissue's intrinsic properties and deflection of the double cone and intermedialia  
412 structure, i.e., the continuum structural modulus.

413           Porter et al. (2014) studied in vivo and in situ strains of dogfish vertebrae using  
414 sonomicrometry. During low velocity swimming, compressive and tensile strains up to 2% were  
415 observed; post mortem ex vivo experiments imposing curvatures seen in steadily swimming  
416 dogfish revealed tensile strains approaching 4%. Ingle et al. (2018) performed cyclic  
417 compressive testing on vertebrae from carcharhiniforms and lamniforms and found anterior  
418 vertebrae had lower continuum moduli than posterior vertebrae; in all cases these moduli were  
419 less than 10 MPa. In three-point bending, more closely approximating loading in vivo than  
420 simple compression, Long et al. (2011) measured the apparent storage and loss moduli ( $E'$  and

421 E', respectively) of segments of multiple shark vertebrae. Depending on the amplitude of  
422 maximum curvature, the elastic portion of the modulus E' was between 0.3 and 1.3 MPa, for a  
423 fast swimming carcharhiniform species and 0.1 and 0.6 MPa for a carcharhiniform species  
424 known less for its speed and more for its maneuverability.

425

#### 426 Blue shark

427 Interpretation of EDD intensity maps from the carcharhiniform centrum (blue shark) is  
428 much more straightforward than for the lamniform centrum (shortfin mako). Most of the centrum  
429 volume outside of the double cones of carcharhiniforms is occupied by four wedges (Fig. 1) with  
430 uniform microstructure down to the 15-25  $\mu\text{m}$  level over millimeter lengths (Morse et al. 2022).  
431 Cone walls are multiple EDD voxels thick. Away from the edges of the cone walls, therefore,  
432 changes in diffracted intensity (greater than random variation) must result from differences in  
433 crystallographic texture.

434 As shown in Fig. 5 of the blue shark, bioapatite *c*-axes within the cone walls are strongly  
435 aligned laterally (i.e., along radii from the axis of the centrum), and the *c*-axes within the  
436 intermedialia are aligned axially. If the variation elastic properties with texture of sharks'  
437 mineralized cartilage resembles those of bone, something reasonable to assume for bioapatite-  
438 collagen based natural composites, then the strong *c*-axis directionality in the blue shark centrum  
439 (Fig. 5) corresponds to directional differences in elastic constants. In the cortices of human long  
440 bones, for example, bioapatite *c*-axes tend to be oriented along the axis of the bone, and elastic  
441 moduli for longitudinal vs transverse anatomical orientations are 1.8x greater for the former than  
442 the latter (Guo 2001). Park et al. (2022a) showed sharper *c*-axis texture in tissue cut from shark  
443 centra (both lamniforms and carcharhiniforms) than is observed in bone, and we hypothesize that

444 spatial/directional variation of moduli may be more pronounced in the mineralized shark centra  
445 than in long bones. If, like in bone, it is correct to infer increased stiffness along directions where  
446 *c*-axes are concentrated, then it appears that the mineral in the carcharhiniform cone walls is  
447 aligned to resist lateral deflections and that the mineral in the intermedialia is aligned to resist  
448 axial compression. 3D numerical models could confirm or refute this conjecture by incorporating  
449 elastic constants consistent with the 3D EDD maps with geometry derived from lab microCT of  
450 centra.

451         In Fig. 4 (reflection *q* of the blue shark centrum), comparison of the intensity map of  
452 detector 5 vs detector 1 (or 9) shows a difference of intensity only in the small sector oriented at  
453 11 o'clock; however, the intensity map of the 11 o'clock section for detector 10 (diametrically  
454 opposite of detector 5) does not differ from those of detectors 1 (or 9). On balance, reflection *q*  
455 of the blue shark reveals weak texture, not unlike the weak texture seen for this set of reflections  
456 in mineralized tissues based on a type I collagen matrix (bone, dentin, cementum) reinforced  
457 with bioapatite, i.e., Almer and Stock (2005), Stock et al. (2014), Ryan et al (2020), Park et al.  
458 (2022b).

459

#### 460 Shortfin mako

461         The EDD maps of the shortfin mako centrum (Fig. 6) cover only part of the intermedialia  
462 and none of the cone wall; because the lamellae were so narrow, this choice was made to obtain  
463 highest spatial resolution in the available beam time. One cannot compare, therefore, the texture  
464 of the cone walls with that of the lamellae for this data set. If the mako intermedialia texture  
465 were the same as in the blue shark intermedialia, the 00.2 intensities of detectors 1 and 9 would  
466 be substantially larger than those in detectors 5 and 10. The situation, however, appears more

467 complicated in the shortfin mako centrum: the 00.2 intensities of detector 5 and 9 are  
468 comparable, that of detector 1 is the largest of all detectors and that of detector 10 is substantially  
469 lower than any other detector. Note also that the detectors with an upward component (1-4) have  
470 higher intensities than those with a downward component (6-9).

471         The reduced axial orientation in the intermedialia of the shortfin mako compared to that  
472 of the blue shark tempts one to speculate that mechanical loading of the lamellae differs from  
473 that of the wedges and that this drives the difference in *c*-axis orientation (and in the underlying  
474 cartilage). Lamellae must resist out of plane bending produced by applied axial compression.  
475 The situation is further complicated by the fact that lamellae experience reactionary axial tensile  
476 loading when opposite side of the centrum is compressed. With multiaxial resistance required,  
477 one would expect the *c*-axes of growing mineralized tissue to be laid down in more isotropic  
478 orientations. In contrast, most of the wedge volume in carcharhiniforms has pronounced lateral  
479 constraint from the surrounding material, and one would expect axial reinforcement is the main  
480 requirement on the mineral phase. However attractive this speculation is, it needs to confirmed  
481 by improved measurements.

482         For the shortfin mako centrum, the quadruplet reflections show some intensity variation  
483 between maps with different detectors (Fig. 6). Like that seen in the 00.2 maps, detector 5  
484 intensity is greater than detector 10. In Fig. 6, detectors 4-6 also have greater intensities than  
485 detectors 1-3 and 7-9. The quadruplet reflection for the shortfin mako centrum, therefore, is more  
486 revealing of texture than the same reflection in bone. This is not unexpected because the matrix  
487 of shark centra is cartilage (and not type I collagen), and WAXS and SAXS of blocks of tissue  
488 cut from centra showed organization of the bioapatite nanoparticles a bit different from that in  
489 bone (Park et al. 2022a).

490           The authors anticipated that the relatively large sampling volume length along the beam  
491 direction and the narrow width of the lamellae in the shortfin mako intermedialia (Fig. 1) would  
492 complicate analysis and therefore concentrated available scanning time on sampling with a much  
493 finer grid over a much smaller volume than in the blue shark. Despite this, interpretation of the  
494 shortfin mako EDD data is still confounded by sub-voxel sampling: in some positions it appears  
495 two, three or more lamellae contribute intensities and nearby voxels only one lamella  
496 contributes. Three radial bands (red arrows at the bottom of Fig. 6a) are structures where  
497 individual lamellae or pairs of lamellae are sampled whereas the bands bordering the gaps are  
498 examples of signals from larger groups of lamellae combined in a single EDD voxel. As it is  
499 unlikely that EDD mapping with isotropic 100  $\mu\text{m}$  voxels will be achieved in the near future,  
500 interpretation of data from lamniform centra will require care and be circumscribed with caveats  
501 whereas analysis of carcharhiniform centra should be straightforward. Accurate registration of  
502 lab microCT and EDD reconstructions could offer a way forward in studying lamniform  
503 intermedialia, but implementing, validating and applying such methodologies is apt to be  
504 extremely laborious.

505

#### 506 *In situ EDD strain mapping of centra*

507           The studies cited above (Porter and Long 2010, Long et al. 2011, Porter et al. 2014, Ingle  
508 et al. 2018) demonstrated shark centra experience large continuum level strains in vivo but did  
509 not reveal (a) whether the mineral and not merely the type II cartilage was deforming nor (b)  
510 whether, if the mineral phase does carry strain, this strain varies as a function of position. Stock  
511 et al. (2022) used synchrotron microCT to show that cone walls and intermedialia consisted of  
512 thin, closely-spaced trabeculae with a substantial volume fraction of unmineralized tissue.

513 Concerning question (a), Stock et al. (2021) found that a polymer matrix composite containing a  
514 very large volume fraction of synthetic hAp particles and an open framework of struts  
515 experienced large structural distortions (engineering strains > 20%) without hAp carrying  
516 appreciable strain. Regarding question (b), Park et al. (2022c) presented a preliminary report of  
517 EDD-derived strain maps in a shark centra under compression but did not report detailed  
518 analyses.

519       Use of purpose-built load frames for tomography studying specimens under load, e.g.  
520 Breunig et al. (1992, 1993), and position-resolved strain quantification under applied load for  
521 mineralized tissues, e.g. Almer and Stock (2010), Stock et al. (2011), are not new, but the  
522 approach of Park et al. (2022c) is novel because EDD is used and because these are the first  
523 positioned resolved and in situ strain measurements for shark mineralized tissue. In this proof of  
524 principle experiment, Park et al. used spacers within a plastic jar, between jar's lid and base, to  
525 compress the centra by known increments. The sampling volume was scanned across the middle  
526 transverse plane of the centra with no applied displacement and after one increment of  
527 compression. Changes in diffraction peak positions for the detector pair 5 and 10 and for pair 1  
528 and 9 are the basis for the strain determination, a standard x-ray diffraction approach, and Park et  
529 al. (2022c) found shifts in bioapatite peak positions for different displacements, indicating the  
530 mineral phase was being strained. Work remains before 3D maps of strain distributions are  
531 extracted.

532

### 533 Modeling of centra response to loading

534       The authors are unaware of any 2D or 3D modeling of shark centra response to  
535 deformation. Mineralized shark cartilage, however, has been modeled numerically for several

536 interconnected tesserae (Seidel et al. 2019). The tesserae modeling was 2D and considered two  
537 structural units: stiffer, more highly-mineralized, radially-oriented spokes and inter-spoke  
538 volumes. Synchrotron microCT of centra (Stock et al. 2022) indicates the micrometer-level  
539 structure of centra is quite different from that of tesserae, so the results of Seidel et al. (2019) are  
540 not directly transferrable to centra. MicroCT-based, 3D models of trabecular bone and of antler  
541 are well developed, e.g., Kinney et al. (2000), Niebur et al. (2000), van Rietbergen (2001), Gupta  
542 et al. (2013), and use of these approaches might be very valuable with centra.

543         Modeling shark centra is outside of the areas in which the authors work. However, the  
544 available macrostructural, microstructural, mineral density and crystallographic texture data  
545 suggest differences, particularly between cone and wedge, evolved to provide improved  
546 mechanical functionality. The authors propose the following sequence of simple-to-complex  
547 models (Fig. 7) as an effective approach. For purposes of illustration, the present discussion is  
548 restricted to the more geometrically simple carcharhiniform centra (intermedialia consisting of a  
549 pair of large medio-lateral wedges and a pair of dorsal-ventral wedges) and ignores lamniform  
550 centra (intermedialia consisting of closely-spaced, diverging and merging lamellae), see Morse et  
551 al. (2022).

552         A first step could be 2D simplifications based on the diametral section through the center  
553 of medio-lateral wedges (locations at “xs” in the middle panels of Fig. 7a-c and sections shown  
554 in the bottom panels of Fig. 7a-c). This section is the one that would experience the largest range  
555 of in vivo strains. The simplest loading regime is uniaxial compression, applied load P, and  
556 simplest centrum model consists of three materials (Fig. 7a): unmineralized cartilage “uc” of the  
557 gap regions between wedges (“g” in Fig. 1), mineralized cartilage “mc” of the centrum (ignoring  
558 differences in mineralization levels between cone and intermedialia) and intervertebral fluid



559 “ivf” (incompressible, sealed in the volume between cones of adjoining centra). In the 2D model,  
560 one could investigate the effect of mineralized cartilage’s (isotropic) Young’s modulus on strain  
561 distribution. Different hourglass angles  $\alpha$ , centrum heights  $h$  and diameters  $\phi$  occur along the  
562 length of the shark vertebral column and for different carcharhiniform species (Ingle et al. 2018,  
563 Morse et al. 2022), and the effect of these on strain distributions can also be examined  
564 parametrically. Simple uniaxial compression of the same three-component model can be  
565 extended to a distribution of loads representing in vivo bending (bottom panel, Fig. 7b).

566         The next level of complexity for a 2D model is partitioning the mineralized cartilage into  
567 cone “c” with thickness  $\delta$  and intermedialia “i” with isotropic Young’s moduli  $E_c$  and  $E_w$ ,  
568 respectively. Although centra tissue moduli data do not presently exist, one expects  $E_c > E_w$   
569 because carcharhiniform cones contain more mineral than their intermedialia (Morse et al. 2022),  
570 and, as a zero-order approximation, one expects a relationship between tissue mineral level and  
571 Young’s modulus similar to that in bone (Currey 2002). Different combinations of  $\alpha$ ,  $h$ ,  $\phi$  and  $\delta$   
572 could be examined virtually and compared to what nature has evolved.

573         Centra are 3D structures, and the 2D models would not be expected to capture all aspects  
574 of deformation. The 3D macrostructure can be imported into a finite element or other numerical  
575 model using 3D microCT data, e.g. Morse et al. (2022). As mentioned above, this approach is  
576 widely applied for trabecular bone, and a sampling of such studies can be found elsewhere  
577 (Stock 2019). Following the steps outlined above in 2D, a three-component, two-material system  
578 with isotropic Young’s moduli would be modeled first in uniaxial compression (Fig. 7a, top) and  
579 then in bending (Fig. 7b, top). Note that  $E_{mc} \gg E_{uc}$ , where mc and uc denotes the mineralized  
580 and unmineralized cartilage, respectively. One expects a slight variation in strains between the

581 the wedge interiors to the volumes bordering the gaps containing unmineralized cartilage. It  
582 would also be interesting to see whether strain varied radially and axially within the wedge.

583 The next step might be partition of the mineralized tissue into cone and intermedialia  
584 with isotropic Young's moduli  $E_c > E_w$ . In addition to the spatial variations mentioned in the  
585 previous paragraph, strain gradients may occur between cone and intermedialia.

586 Based on the EDD observations reported above, namely, that strong bioapatite *c*-axis  
587 crystallographic textures occur in the cone and intermedialia, the authors believe that accurate  
588 modeling will require anisotropic moduli for both structures. In the centrum's coordinate system  
589 of tangential, radial and axial directions, denoted *t*, *r* and *a*, respectively (Fig. 7d), the anisotropic  
590 Young's moduli are denoted  $E_t$ ,  $E_r$  and  $E_a$ , , respectively. More experimental work is required to  
591 determine how much  $E_t$ ,  $E_r$  and  $E_a$  actually differ, but this could be examined virtually via the 3D  
592 model.

593

594

#### 595 *Alternatives to EDD and future experiments*

596 Alternatives to EDD exist which are suitable for samples containing nanocrystals (such as  
597 are present in bioapatites), which employ monochromatic x-radiation and which might allow  
598 diffraction from an individual lamella to be isolated from that of closely spaced neighbors. Use  
599 of conical slits (Park et al. 2013) or spiral slits (Martins et al. 2010) with monochromatic x-rays,  
600 for example, allows diffraction patterns to be collected with a simple area detector and would not  
601 require a specialized detector array. Translation similar to that employed here would allow 3D  
602 reconstruction of the volume, but the sampling volume would be elongated along the beam  
603 direction like that in the present study. Insertion devices such as that of 1-ID, APS, presently

604 offer orders of magnitude greater flux at any selected wavelength compared to 6-BM-B, and the  
605 greater flux could be traded for finer spatial sampling. Conical slits tailored for monochromatic  
606 x-rays and the hexagonal crystal system (i.e., for bioapatites) do not appear to exist, limiting the  
607 number of diffraction peaks which can be collected simultaneously, but spiral slits can capture  
608 all of the hexagonal reflections at the same time albeit with azimuthal gaps in the diffraction  
609 rings. It is, however, extremely difficult to obtain beam time at 1-ID, APS, so EDD at 6-BM-B,  
610 APS, remains an extremely attractive option.

611 An alternative to slit-based approaches is x-ray diffraction tomography with an incident  
612 monochromatic pencil beam, an open area detector and translation-rotation data acquisition, e.g.  
613 Stock et al. (2008), Birkbak et al. (2015). Reconstruction of cross-sectional variation of  
614 diffracted intensity employs back projection or other computed tomography algorithm.  
615 Compared to the translation-rotation method, 3D EDD mapping has the advantage of isolating  
616 diffraction from the sampling volume from all other scattering. Additionally, EDD mapping does  
617 not require specimen rotation, and specimens with complex surrounding tissue can be aligned so  
618 these structures do not affect the diffraction signal. For completeness, one should mention the 3D  
619 scattering approach termed tensor tomography which has been applied to bone, e.g. Maleki et al.  
620 (2014), but only to relatively small sections cut from larger specimens.

621 Accumulated x-ray damage affects mechanical properties of collagen-based mineralized  
622 tissues (Barth et al. 2011), these effects rise with increasing dose and become a concern in the  
623 context of in situ loading and strain measurements. While estimating dose is fairly  
624 straightforward with monochromatic high-energy x-rays, e.g., Stock et al. (2020), quantitative  
625 estimates for polychromatic x-radiation cannot currently be made mainly because incident x-ray  
626 spectra (intensity vs energy) are unavailable for the 6-BM-B bending magnet. Were the spectra

627 available, one could then calculate dose for each energy using tabulations such as that of Hubble  
628 and Seltzer (2004) and sum the individual contributions.

629         In qualitative terms, 3D mapping with EDD damages the tissue much more than the  
630 monochromatic, high-energy techniques described above; this may not be an issue for one-and-  
631 done mapping (like the data reported above) but might be for in situ loading experiments. First,  
632 photons in the 25-55 keV range (the EDD data) deposit much more energy per photon those at  
633 70 keV and above. Second, in monochromatic methods, all of the photons traversing the  
634 specimen have the potential to contribute to the diffracted signal whereas in EDD, photons with  
635 energies between those diffracted into the detectors, deposit energy in the specimen and do not  
636 contribute to signal. Third, all points along the path of the incident beam are exposed when  
637 diffraction from one sampling volume is collected: If ten positions through the sample thickness  
638 are sampled, then the dose is ten time larger over the entire thickness.

639         Some damage to mineralized tissue samples is inevitable for x-ray-based methods such as  
640 diffraction, and damage is minimized if each sampled volume is exposed once for the minimum  
641 time required to obtain useful signal. In diffraction quantification of internal strains  
642 accompanying four-point bending, for example, Gallant et al. (2014) made use of the fact that the  
643 tensile to compressive strain gradients are nominally the same for all cross-sections within the  
644 inner span of the apparatus; they translated to a new cross-section before measuring strains for  
645 each increment of deflection. This approach could be adapted for EDD mapping of the  
646 intermedialia of carcharhiniform centra where strains should vary continuously. With reference  
647 to Fig. 2d, one could collect data at the red squares' positions for one increment of deformation  
648 and then at an adjacent position for the next.

649 The preliminary report of Park et al. (2022c) suggests in situ compression and EDD 3D  
650 mapping of strains in the bioapatite phase of shark centra will be very informative in describing  
651 how the centra function mechanically. It should be straightforward use EDD to apply x-ray  
652 diffraction strain quantification under four-point bending (e.g. Gallant et al. 2014) to segments of  
653 multiple shark vertebrae (e.g. Long et al. 2011), i.e., in a loading mode more closely  
654 approximating that in vivo.

655  
656 **CRedit authorship contribution statement** J.S. Park: Writing – review & editing,  
657 Visualization, Methodology, Formal analysis. H. Chen: Writing – review & editing, Software,  
658 Methodology. K.C. James: Writing – review & editing, Resources, Methodology. L.J. Natanson:  
659 Writing – review & editing, Resources, Methodology. S.R. Stock: Writing – review & editing,  
660 Writing – original draft, Visualization, Validation, Supervision, Resources, Project  
661 administration, Methodology, Investigation, Funding acquisition, Formal analysis, Data curation,  
662 Conceptualization.

663 **Declaration of competing interest** The authors declare that they have no known  
664 competing financial interests or personal relationships that could have appeared to influence the  
665 work reported in this paper.

666 **Data availability** Data will be made available on request.

667

## 668 **Acknowledgements**

669 Beamline 6-BM-B, APS, is supported by COMPRES, the Consortium for Materials  
670 Properties Research in Earth Sciences under NSF Cooperative Agreement EAR-1661511. This  
671 research used resources of the Advanced Photon Source, a U.S. Department of Energy (DOE)

672 Office of Science User Facility, operated for the DOE Office of Science by Argonne National  
673 Laboratory under Contract No. DE-AC02-06CH11357. Argonne National Laboratory's work was  
674 supported by the U.S. Department of Energy, Office of Science, Office of Basic Energy  
675 Sciences, under contract DE-AC02-06CH11357.

676

677 [Appendix A. Supplementary data](https://doi.org/10.1016/j.jmbbm.2022.105506) Supplementary data to this article can be found online at  
678 <https://doi.org/10.1016/j.jmbbm.2022.105506>.

679

## 680 **References**

681

682 Almer, J.D., Stock, S.R. 2005. Internal strains and stresses measured in cortical bone via high-  
683 energy x-ray diffraction. *J Struct Biol* **152**, 14-27.

684 Almer, J.D., Stock, S.R. 2010. Loading-related strain gradients spanning the mature bovine  
685 dentinoenamel junction (DEJ): Quantification using high energy x-ray scattering. *J Biomech*  
686 **43**, 2294-2300.

687 Barth, H.D., Zimmermann, E.A., Schaible, E., Tang, S.Y., Alliston, T., Ritchie, R.O. 2011.  
688 Characterization of the effects of x-ray irradiation on the hierarchical structure and  
689 mechanical properties of human cortical bone. *Biomater* **32**, 8892-8904.

690 Birkbak, M.E., Leemreize, H., Frølich, S., Stock, S.R., Birkedal, H. 2015. Diffraction Scattering  
691 Computed Tomography: A Window into the Structures of Complex Nanomaterials.  
692 *Nanoscale* **7**, 18402 – 18410.

693 Breunig, T.M., Stock, S.R., Antolovich, S.D., Kinney, J.H., Massey, W.N, Nichols, M.C. 1992.  
694 A Framework Relating Macroscopic Measures and Physical Processes of Crack Closure of

695 Al-Li Alloy 2090. in *Fracture Mechanics: Twenty-Second Symposium (Volume 1)*, ASTM  
696 STP **1131** (1992) 749-761.

697 Breunig, T.M., Stock, S.R., Brown, R.C. 1993. Simple Load Frame for in situ Computed  
698 Tomography and X-ray Tomographic Microscopy. *Mater Eval* **51**, 596-600.

699 Chaumel, J., Schotte, M., Bizzarro, J.J., Zaslansky, P., Fratzl, P., Baum, D., Dean, M.N. 2020.  
700 Co-aligned chondrocytes: Zonal morphological variation and structures arrangement of cell  
701 lacunae in tessellated cartilage. *Bone* **134**, 115624.

702 Cullity, B.D., Stock, S.R. 2001. *Elements of X-ray Diffraction*, 3rd Ed., Prentice-Hall: Upper  
703 Saddle River.

704 Currey, J.D. 2002. *Bones – Structure and Mechanics* Princeton: Princeton Univ. Press. Dean,  
705 M.N., Chiou, W.-A., Summers, A.P. 2005. Morphology and ultrastructure of prismatic  
706 calcified cartilage. *Microsc Microanal* **11**, 1196-1197.

707 Gallant, M.A., Brown, D.M., Hammond, M., Wallace, J.M., Du, J., Deymier-Black, A.C.,  
708 Almer, J.D., Stock, S.R., Allen, M.R., Burr, D.B. 2014. Bone cell-independent benefits of  
709 raloxifene on the skeleton: A novel mechanism for improving bone material properties.  
710 *Bone* **61**, 191-200.

711 Geraghty, P.T., Jones, A.S., Stewart, J., Macbeth, W.G. 2012. Micro-computed tomography: an  
712 alternative method for shark aging. *J Fish Biol* **80**, 1292-1299.

713 Gupta, H.S., Krauss, S., Kerschnitzki, M., Karunaratne, A., Dunlop, J.W.C., Barber, A.H.,  
714 Boesecke, P., Funari, S.S., Fratzl, P. 2013. Intrafibrillar plasticity through mineral/collagen  
715 sliding is the dominant mechanism for the extreme toughness of antler bone. *J Mech Behav*  
716 *Biomed Mater* **28**, 366-382.

717 Gupta, H.S., Schratler, S., Tesch, W., Roschger, P., Berzlanovich, A., Schoeberl, T., Klaushofer,  
718 K., Fratzl, P. 2005. Two different correlations between nanoindentation modulus and mineral  
719 content in the bone–cartilage interface. *J Struct Biol* **149**, 138-148.

720 Guo, X.E. 2001. Mechanical properties of cortical bone and cancellous bone tissue. Ch. 10 in  
721 *Bone Mechanics Handbook*, 2<sup>nd</sup> Ed. Cowin, S.C., Ed. Boca Raton (FL), CRC Press, pp 10-1-  
722 10-23.

723 Hubbell, J.H., Seltzer, S.M. 2004. Tables of X-Ray Mass Attenuation Coefficients and Mass  
724 Energy-Absorption Coefficients from 1 keV to 20 MeV for Elements  $Z = 1$  to 92 and 48  
725 Additional Substances of Dosimetric Interest. NISTIR 5632, accessed Aug. 7, 2020.  
726 <https://www.nist.gov/pml/x-ray-mass-attenuation-coefficients>

727 Ingle, D.I., Natanson, L.J., Porter, M.E. 2018. Mechanical behavior of shark vertebral centra at  
728 biologically relevant strains. *J Exp Biol* **221**, 188318.

729 Kinney, J. H., Haupt, D.L., Balooch, M., Ladd, A. J. C., Ryaby, J. T. , Lane, N. E. 2000. Three-  
730 dimensional morphometry of the L6 vertebra in the ovariectomized rat model of  
731 osteoporosis: Biomechanical implications. *J Bone Miner Res* **15**, 1981-1991.

732 Liu, X., Dean, M.N., Youssefpour, H., Summers, A.P., Earthamn, J.C. 2014. Stress relaxation  
733 behavior of tessellated cartilage from the jaws of blue sharks. *J Mech Behav Biomed Mater*  
734 **29**, 68-80.

735 Long, J.H. Jr., Koob, T., Schaefer, J., Summers, A., Bantilan, K., Grotmol, S. Porter, M. 2011.  
736 Inspired by sharks: A biomimetic skeleton for the flapping, propulsive tail of an aquatic  
737 robot. *Marine Technol Soc J* **45**(4), 119-129.



738 Malecki, A., Potdevin, G., Biernath, T., Eggl, E., Willer, K., Lasser, T., Maisenbacher, J.,  
739 Gibmeier, J., Wanner, A., Pfeiffer, F. 2014. X-ray tensor tomography. *Europhys Lett* **105**,  
740 38002.

741 Martins, R.V., Ohms, C., and Decroos, K. 2010. Full 3D spatially resolved mapping of residual  
742 strain in a 316L austenitic stainless steel weld specimen. *Mater Sci Eng A* **527**, 4779–4787.

743 Morse, P.E., Stock, M.K., James, K.C., Natanson, L.J., Stock, S.R. 2022. Shark vertebral  
744 microanatomy and mineral density variation studied with laboratory microComputed  
745 Tomography. *J Struct Biol* **214**, 107831.

746 Naik, N.N., Jupe, A.C., Stock, S.R., Wilkinson, A.P., Lee, P.L., Kurtis, K.E. 2006. Sulfate attack  
747 monitored by microCT and EDXRD: Influence of cement type, water-to-cement ratio, and  
748 aggregate. *Cement Concrete Res* **36**, 144-159.

749 Natanson, L.J., Skomal, G.B., Hoffmann, S.L., Porter, M.E., Goldman, K.J., Serra, D. 2018. Age  
750 and growth of sharks: do vertebral band pairs record age? *Mar Freshwater Res* **69**, 1440-  
751 1452.

752 Niebur, G.L., Feldstein, M.J., Yuen, J.C., Chen, T.J., Keaveny, T.M. 2000. High-resolution finite  
753 element models with tissue strength asymmetry accurately predict failure of trabecular bone.  
754 *J Biomech* **33**, 1575-1583.

755 Park, J.S., Lienert, U., Dawson, P.R., and Miller, M.P. 2013. Quantifying Three-Dimensional  
756 Residual Stress Distributions Using Spatially-Resolved Diffraction Measurements and Finite  
757 Element Based Data Reduction. *Exp Mech* **53**, 1491–1507.

758 Park, J.-S. Almer, J.D., James, K.C., Natanson, L.J., Stock, S.R. 2022a. Mineral in shark  
759 vertebrae studied by wide angle and by small angle x-ray scattering. Under revision.

760 Park, J.-S., Laugesen, M., Mays, S., Birkedal, H., Almer, J.D., Stock, S.R. 2022b. Intact  
761 archeological human bones studied with transmission x-ray diffraction and small angle x-ray  
762 scattering. *Int J Osteoarchaeol* **32**, 170-181.

763 Park, J.S., Chuang, A.C., Okasinski, J., Chen, H., Shade, P., Stock, S.R., Almer, J. A new  
764 residual strain mapping program using energy dispersive x-ray diffraction at the Advanced  
765 Photon Source. 2022c. *Exp Mech*, accepted.

766 Porter, M.E., Long, J.H. Jr. 2010. Vertebrae in compression: Mechanical behavior of arches and  
767 centra in the gray smooth-hound shark (*Mustelus californicus*). *J Morphol* **271**, 366-375.

768 Porter, M.E., Diaz, C., Sturm, J.J., Grotmol, S., Summers, A.P., Long, J.H., Jr. 2014. Built for  
769 speed: strain in the cartilaginous vertebral columns of sharks. *Zool* **117**, 19-27.

770 Porter, M.E., Ewoldt, R.H., Long, J.H. Jr. 2016. Automatic control: the vertebral column of  
771 dogfish sharks behaves as a continuously variable transmission with smoothly shifting  
772 functions. *J Exp Biol* **219**, 2908-2919.

773 Ryan, J., Stulajter, M.M., Okasinski, J.S., Cai, Z., Gonzalez, G.B., Stock, S.R. 2020. Carbonated  
774 apatite lattice parameter variation across incremental growth lines in teeth. *Materialia* **14**,  
775 100935.

776 Seidel, R., Roschger, A., Li, L., Bizzarro, J.J., Zhang, Q., Yin, J., Yang, T., Weaver, J.C., Fratzl,  
777 P. Roschger, P., Dean, M.N. 2019. Mechanical properties of stingray tesseræ: High-  
778 resolution correlative analysis of mineral density and indentation moduli in tessellated  
779 cartilage. *Acta Biomater* **96**, 421-435.

780 Seidel, R., Jayasankar, A.K., Dean, M.N. 2021. The multiscale architecture of tessellated  
781 cartilage and its relation to function. *J Fish Biol* **98**, 942-955.

782 Stock, S.R. 2019. *MicroComputed Tomography: Methodology and Applications*, 2<sup>nd</sup> Ed., Taylor  
783 and Francis.

784 Stock, S.R., DeCarlo, F., Almer, J.D. 2008. High energy x-ray scattering tomography applied to  
785 bone. *J Struct Biol* **161**, 144-150.

786 Stock, S.R., Deymier-Black, A.C., Veis, A., Telser, A., Lux, E., Cai, Z. 2014. Bovine and equine  
787 peritubular and intertubular dentin. *Acta Biomater* **10**, 3969-3977.

788 Stock, S.R., Yuan, Fang, Brinson, L.C., Almer, J.D. 2011. High-energy x-ray scattering  
789 quantification of internal strains and their gradients in bone under load. *J Biomech* **44**, 291-  
790 296.

791 Stock, S.R., Stock, M.K., Almer, J.D. 2020. Combined Computed Tomography and position-  
792 resolved x-ray diffraction of an intact Roman-era Egyptian portrait mummy. *J Royal Soc*  
793 *Interface* **17**, 20200686.

794 Stock, S.R., Park, J.-S., Jakus, A., Birkbak, M., Frølich, S., Birkedal, H., Shah, R., Almer, J.D.  
795 2021. “*In situ* loading and x-ray diffraction quantification of strains in hydroxyapatite  
796 particles within a 3D printed scaffold.” *Materialia* **18**, 101174.

797 Stock, S.R., Morse, P.E., Stock, M.K., James, K.C., Natanson, L.J., Chen, Haiyan, Shevchenko,  
798 P.D., Maxey, E.R., Antipova, O.A., Park, J.-S. 2022. “Microstructure and energy dispersive  
799 diffraction reconstruction of 3D patterns of crystallographic texture in a shark centrum.” *J*  
800 *Medical Imaging* **9**, 031504.

801 Urist, M.R. 1961. Calcium and phosphorus in the blood and skeleton of the Elasmobranchii.  
802 *Endocrinol* **69**, 778-801.

803 van Rietbergen, B. 2001. Micro-FE analyses of bone - State of the art. in Noninvasive  
804 Assessment of Trabecular Bone Architecture and the Competence of Bone. Bay, B.K.,  
805 Majumdar, S. Eds. New York, Kluwer/Plenum. **Adv Exp Med Biol Vol 496**: 21-30.  
806 Watanabe, Y.Y., Lydersen, C., Fisk, A.T., Kovacs, K.M. 2012. The slowest fish: Swim speed  
807 and tail-beat frequency of Greenland sharks. *J Exp Mar Biol Ecol* **426/427**, 5-11.  
808 Weidner, D.J., Vaughan, M.T., Wang, L., Long, H., Li, L., Dixon, N.A., Durham, W.B. 2010.  
809 Precise stress measurements with white synchrotron x-rays. *Rev Sci Instrum* **81**, 013903.

810  
811 **Figure captions**

812 Fig. 1. Schematics of sharks. (a) Side view of a generalized shark. The blocks within the  
813 silhouette represent the vertebrae: gray for cervical and thoracic vertebrae and black for  
814 abdominal vertebrae. The arrow indicates very approximately the position of the vertebrae in this  
815 study. (b) Schematic from above of vertebral compression when a shark swims, illustrated  
816 schematically by three positions of the tail. When the tail swings to the right (right tail diagram),  
817 the right side of the vertebra is compressed (right trapezoid with arrows indicating compression).  
818 As the left side of the schematic indicates, the vertebra's opposite (left) side compresses when  
819 the tail moves to the left. Panels (c) and (d) show lamniform (left column) and carcharhiniform  
820 (right column) abdominal centra. (c) 3D representation of a lamniform and a carcharhiniform  
821 centrum with some material shown transparent so that the structures' cross-sections can be seen.  
822 c - hourglass-shaped cone walls, i – intermedialia, L – lamella, W – wedge. (d) Thresholded  
823 slices (black in these transverse sections perpendicular to the vertebral column axis and near the  
824 centra's axial midplane) of a mako centrum (lamniform shark mapped in this study) showing the  
825 radial lamellae and of a sandbar shark centrum (carcharhiniform shark similar to the blue shark  
826 mapped in this study). The dorsal-ventral plane is vertical (double arrowed line), and the

827 intersection of the frontal (coronal) plane with each slice is shown as a horizontal red dotted line.  
828 Gaps “g” between wedges (sandbar shark) and between groups of closely spaced lamellae (mako  
829 shark) are labeled.

830 Fig. 2. Schematic of the EDD apparatus with the arrangement of ten detector elements and of  
831 the sampling scheme illustrated for a lamniform and a carcharhiniform shark. (a) Energy  
832 dispersive diffraction apparatus illustrated with a schematic of a lamniform centrum. A set of  
833 three orthogonal linear translators (along X, Y and Z) scan the specimen across the sampling  
834 volume “sv”. The other main components are: detector elements “de”, conical slits “cs” and  
835 incident beam collimator “col”. (b) Arrangement of detector elements 1-10 and the orientation of  
836 different lattice plane normals  $\mathbf{N}_1$  and  $\mathbf{N}_5$  for the crystallites producing diffracted intensities  
837 measured in detectors 1 and 5. (c) Schematic of shortfin mako and (d) diagram of blue shark  
838 sampling grids illustrated by side views (top) and transverse views (bottom) of the two centra.  
839 The labels are: cone wall “cw”, lamellae “L”, wedge “W” and vertebral column axis “vca”. Note  
840 that only a small portion of the shortfin mako centrum was covered, but the entire volume of the  
841 blue shark centrum was scanned.

842 Fig. 3. Typical energy dispersive diffraction pattern from a shark centrum. The 00.2 and “q”  
843 (unresolved 21.1, 11.2, 30.0 and 20.2) peaks from hAp are labeled as well as peaks “cal” from  
844 the calibration source. The green peaks below the data are for a synthetic hAp reference pattern  
845 (Powder Diffraction File 86-1201).

846 Fig. 4. Orthogonal sections through the blue shark centrum reconstructed with the integrated  
847 intensity of the quadruplet reflection (21.1+11.2+30.0+20.2). The brighter the pixel, the higher  
848 the intensity in the voxel. The number in the upper left of each panel identifies the detector  
849 number. The gray scale images of the top row show intensities recorded with detector 5 (left) and

850 the diametrically opposite detector 10 (middle) and of the bottom row intensities from detectors  
851 1 (left) and diametrically opposite 9 (right). The color panels (right column) show the combined  
852 intensities of detectors 5 and 10 (top) and 1 and 9 (bottom) with 5 and 9 in blue and 10 and 1 in  
853 red. The yellow arrowheads identify the cone wall diffracting greater intensity than the adjacent  
854 intermedialia. The orange arrowheads show portions of the maps where intermedialia and cone  
855 wall intensities are comparable. The yellow (and one black) boxes in the detector 5 and 1 panels  
856 indicate the positions of 3 voxel x 3 voxel x 1 voxel regions used to measure mean diffracted  
857 intensity within the cone wall ( $cw$ ) and intermedialia ( $i, i'$ ); these values are reported in Table 2.

858 Fig. 5. (a) Orthogonal sections through the blue shark centrum reconstructed with the 00.2  
859 integrated intensity. The brighter the pixel, the higher the intensity in the voxel. Intensities from  
860 detectors 5 (blue), 7 (green) and 9 (red) are combined. The different colored arrows show the  $c$ -  
861 axis orientation measured by each detector. (b) Schematic of the bioapatite  $c$ -axis orientations  
862 revealed in panel a. The white boxes indicate the positions of 3 voxel x 3 voxel x 1 voxel regions  
863 used to measure mean diffracted intensity within the cone wall ( $cw$ ), intermedialia ( $i, i'$ ) and  
864 fluid ( $f$ ) for detectors 1 and 5; these values are reported in Table 2.

865 Fig. 6. Shortfin mako's spatial distribution of diffracted intensity measured with the ten  
866 detectors for the quadruplet  $q$  (a) and 00.2 (b) reflections. The color bar between the panels gives  
867 the intensity range which was 0 to 1,200 a.u. for  $q$  and 0-150 for 00.2. The detector data are  
868 placed in their correct relative orientations. The transverse section is from near the centrum's  
869 axial center and covers only part of the cross-section. Portions of two gaps ( $g1$  and  $g2$ ) and of  
870 three sectors ( $s1, s2$  and  $s3$ ) are labeled in the detector 1 map of (a) as is the 2 mm scale bar  
871 (white bar at the bottom). The segmented image inset in the middle of (a) is a lab microCT slice  
872 of the same centrum (from Morse et al. 2022).

873 Fig. 7. Illustration of how carcharhiniform centra data could be incorporated into  
874 numerical models of mechanical response to loading. Centra 3D macroarchitecture from lab  
875 microCT (e.g. Morse et al. 2022) would be converted into a 3D model of the structure.  
876 Incompressible intervertebral fluid (ivf) would fill the space between the cones and the rigid  
877 platens applying load  $P$ . (a) Simple uniaxial compression of centra simplified to contain two  
878 isotropic phases: mineralized cartilage (mc, dark gray) and unmineralized cartilage (uc, light  
879 gray). The magenta arrows (xs) mark the position of the cross-section shown at the bottom of the  
880 panel. The centrum geometry is defined by diameter  $\phi$ , height  $h$  and hourglass angle  $\alpha$ . (b)  
881 Distribution of loads for simulated bending. The location of two large and two small wedges  
882 beneath the cone are shown in yellow, and the largest load occurs at the center of the outer edge  
883 of the large wedges, mimicking in vivo bending. Here the wedge and cone materials are not  
884 differentiated. (c) Non-uniform loading and partition of the mineralized cartilage into cone “c”  
885 (with thickness  $\delta$ , shown in black) and intermedialia “i” (bottom panel). The corresponding 3D  
886 model (top panel) includes unmineralized cartilage “uc”, the intermedialia is in the form of  
887 wedges “W” and isotropic Young’s moduli  $E_c > E_W \gg E_{uc}$ . (d) Transverse centrum cross-section  
888 at the axial position between the cone apex and its axial end. The radial  $r$ , tangential  $t$  and axial  $a$   
889 directions are indicated as are the potentially differing Young’s moduli along these three  
890 directions. The text at the bottom of the panel indicates expected relative magnitudes of moduli  
891 along different directions for the wedge and cone; this is based on the  $c$ -axis crystallographic  
892 textures reported in this paper.

|893

894 Table 1. Experimental parameters

895

896

Shark	Gage volume (mm)			Step size (mm)			Number of steps			exposure (s)
	$\delta X$	$\delta Y$	$\delta Z$	$\Delta X$	$\Delta Y$	$\Delta Z$	$N_x$	$N_y$	$N_z$	
Mako	0.2	0.2	2.5	1.5	0.5	1.0	3	10	47	50
Blue	0.1	0.2	1.7	2.0	1.0	1.9	16	10	17	30

897

898

899

900

901

902

903

904 Table 2. Integrated intensities in the cone wall (cw) and intermedialia (i) of the q and 00.2 reflections for  
 905 the blue shark centrum. Mean values are for the 3 voxel x 3 voxel regions within the yellow squares of  
 906 Fig. 4 and Fig. 5. The standard deviation of each mean is the number following  $\pm$ . The maximum  
 907 integrated intensity of the 3D reconstructed volume with q reflection was 98 (arbitrary units) and with the  
 908 00.2 reflection was 86 (arbitrary units, a.u.). For 00.2, the integrated intensity recorded within fluid-filled  
 909 volumes were 2 a.u. for detectors 1 and 5, and, for q, values were 2 and 4 a.u., respectively.

910

911

Reflection	detector 5		detector 1		
	<i>cw</i>	<i>i</i>	<i>cw</i>	<i>i</i>	<i>i'</i>
q	$68 \pm 7$	$61 \pm 9$	$66 \pm 7$	$46 \pm 10$	$72 \pm 3$
00.2	$46 \pm 9$	$5 \pm 1$	$21 \pm 5$	$35 \pm 2$	

912

913

914

915

916

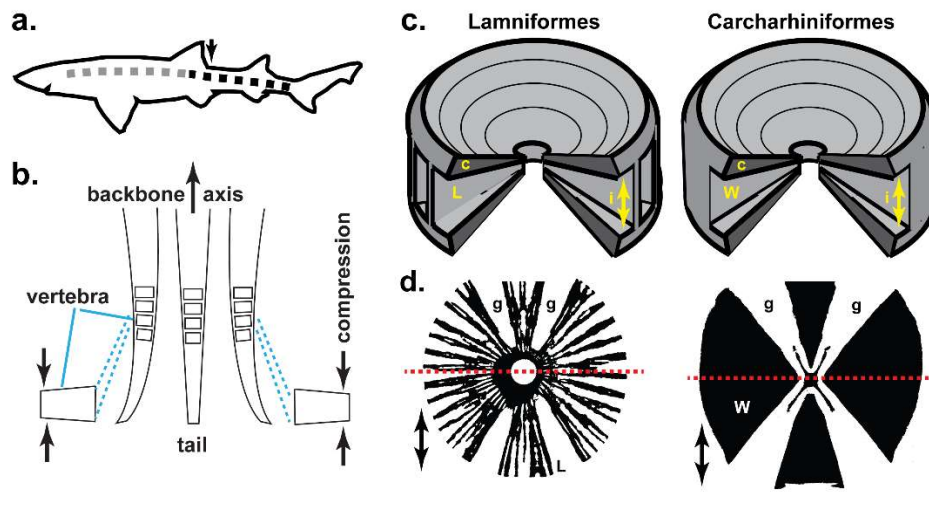
917

918

919

920

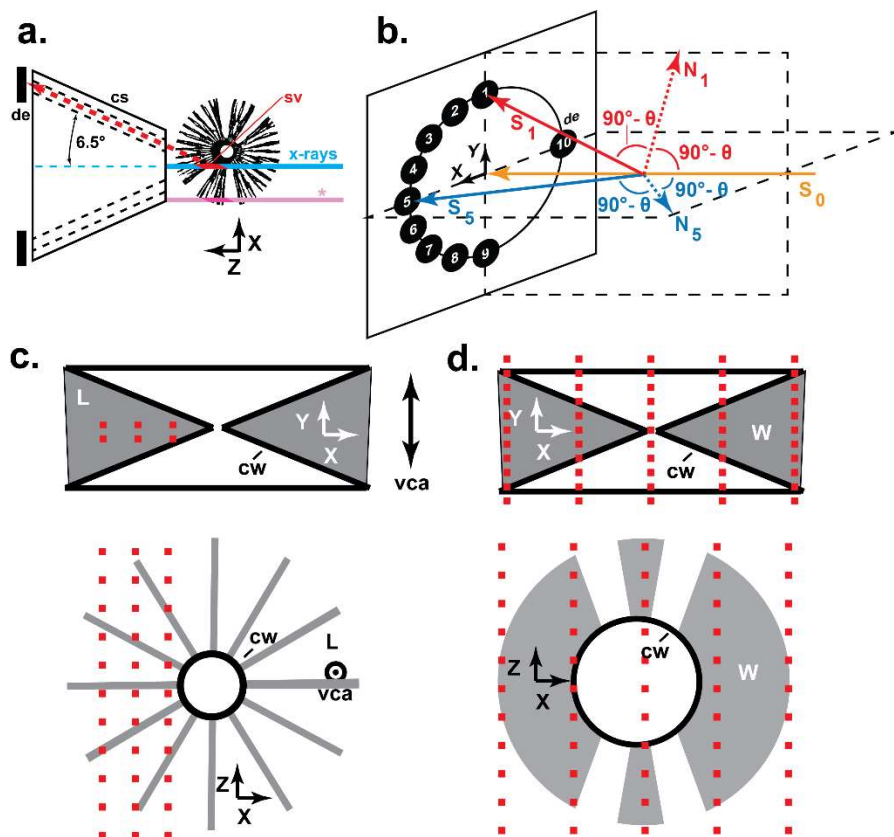
921 Figure 1.





923

Figure 2.

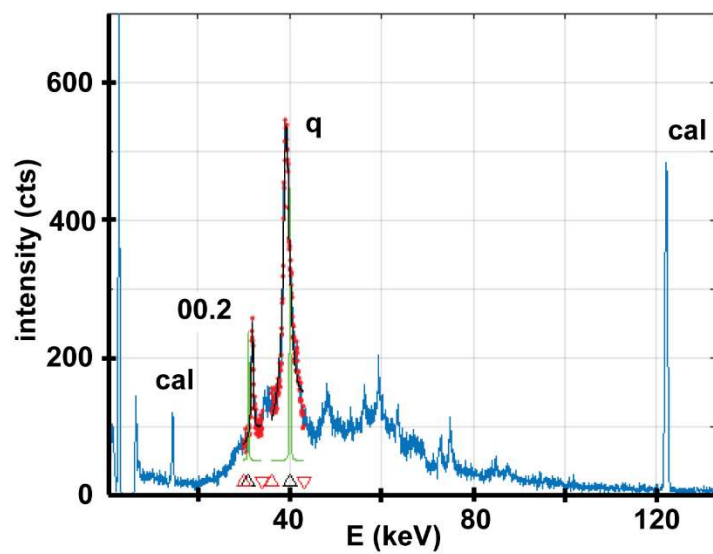


924

925

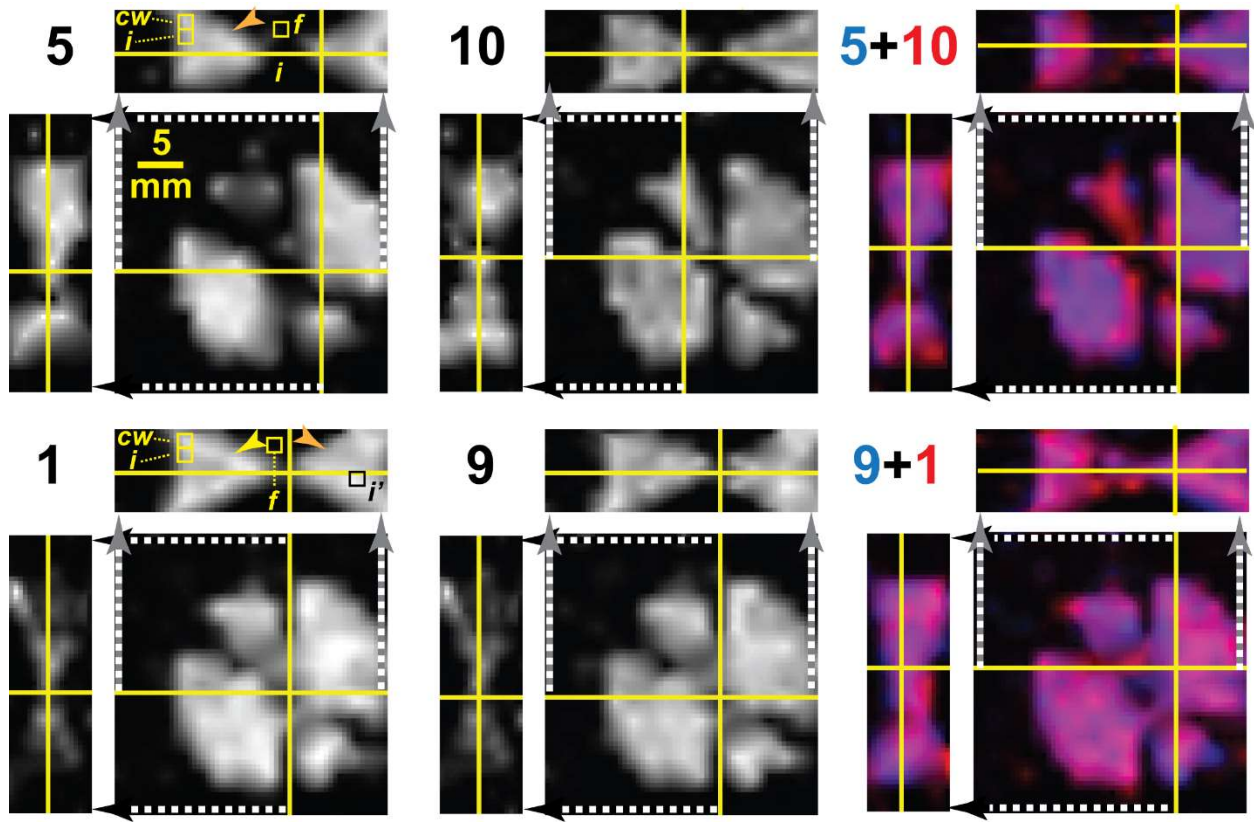
926

Figure 3.



927

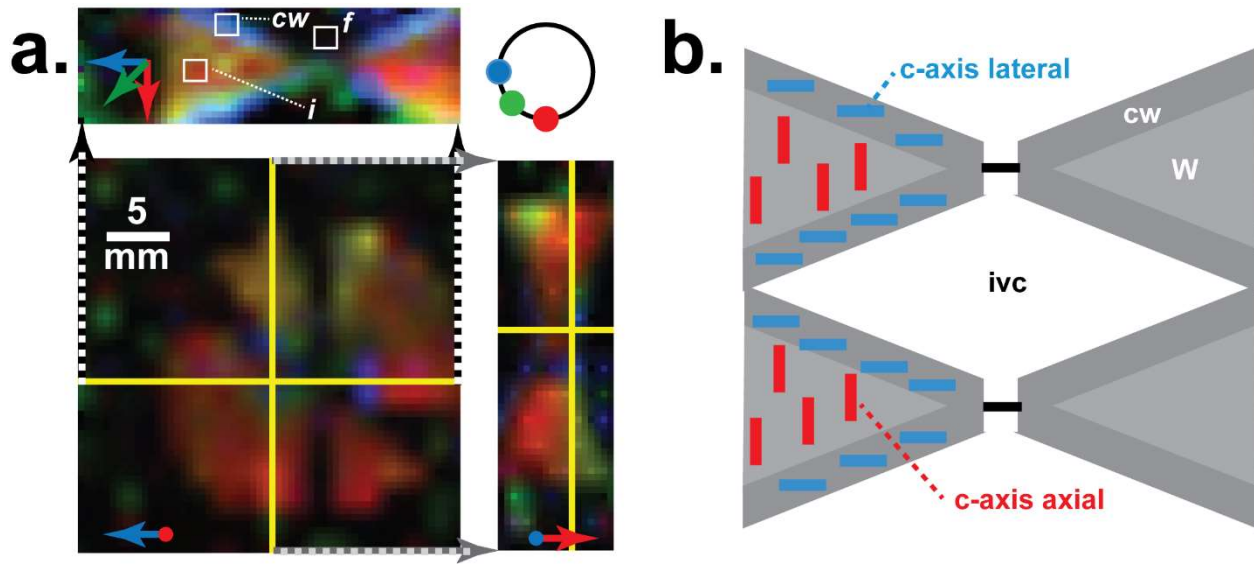
928 [Figure 4.](#)



929

930

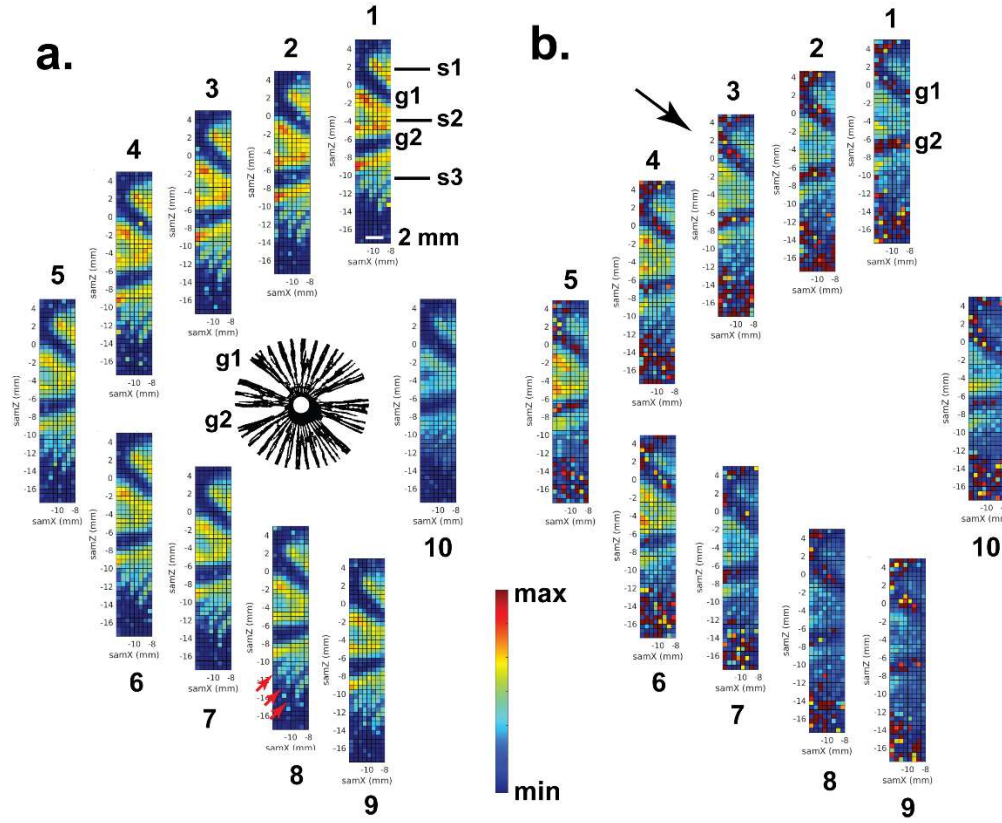
931 [Figure 5.](#)



932

933

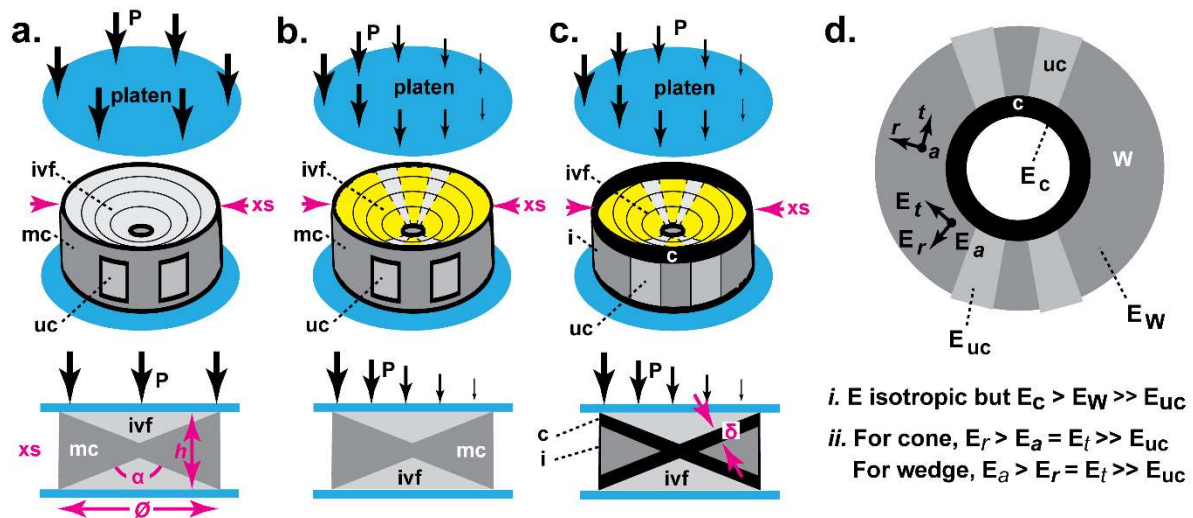
934 Figure 6.



935

936

937 Figure 7.



938